Atmospheric
Chemistry
and Physics

Open Access

EGU

Supplement of

Satellite soil moisture data assimilation impacts on modeling weather variables and ozone in the southeastern US – Part 1: An overview

Min Huang et al.

Correspondence to: Min Huang (mhuang10@gmu.edu)

S1. Additional information on the Noah land surface model and its offline spin-up

Noah version 3.6 was implemented in this study. This version of Noah is similar to Noah version 3.3 (Huang et al., 2017b, 2018), except that snow physics is based on the University of Arizona scheme (Wang et al., 2009). An offline Noah simulation was performed within LIS prior to all WRF-Chem simulations for equilibrated land conditions, covering the period of 1999-2019. The "mean-state" approach (Rodell et al., 2005) was adopted to initialize Noah after cycling the model twice during this entire period. The 1/8° North American Land Data Assimilation System Phase 2 (NLDAS-2, https://ldas.gsfc.nasa.gov/nldas/v2/forcing) was used as the meteorological forcing for this offline spin-up. Most forcing fields of the NLDAS-2 were derived from the North American Regional Reanalysis, which is generally drier and warmer than observations (e.g., Royer and Poirier, 2010; Kennedy et al., 2011).

Surface exchange coefficient C_H is a critical parameter controlling energy transport from the land surface to the atmosphere. It is directly related to the land-atmosphere coupling strength. In Noah, C_H is represented by Equations (S1) and (S2), which are adapted from Equation (15) in Niu et al. (2011):

$$C_H = \frac{\kappa^2}{[\ln\left(\frac{z}{z_{0m}}\right)-\psi_m\left(\frac{z}{L}\right)+\psi_m\left(\frac{z_{0m}}{L}\right)][\ln\left(\frac{z}{z_{0h}}\right)-\psi_h\left(\frac{z}{L}\right)+\psi_h\left(\frac{z_{0h}}{L}\right)]} \qquad \text{(S1)}$$

where κ is the von Kármán constant, ψ_m and ψ_h are stability correction functions, L is the Monin-Obukhov length, and z is the reference height.

The roughness lengths for heat and momentum z_{0h} and z_{0m} are related based on:

$$z_{0h} = z_{0m}\, e^{-\kappa C\sqrt{Re^*}} \qquad \text{(S2)}$$

where Re^* is the roughness Reynolds number varying with friction velocity and z_{0m}, and $C = 0.1$ by default. This default value of C may be highly unrealistic. For example, LeMone et al. (2008) found that C may be underestimated by a factor of 5 in Oklahoma during warm seasons, resulting in significant biases in modeled energy fluxes which cannot be resolved solely by adjusting the modeled soil moisture and vegetation fields. C should ideally be calibrated for various land cover types or canopy heights based on observations.

S2. Additional information on the Wesely dry deposition scheme

Dry deposition velocity v_d in WRF-Chem's default Wesely scheme (Wesely, 1989) is defined as the reciprocal of the sum of aerodynamic resistance r_a, quasi-laminar sublayer resistance r_b, and surface resistance r_c:

$$v_d = \frac{1}{[r_a+r_b+r_c]} \qquad \text{(S3)}$$

r_a and r_b are both sensitive to surface properties such as surface roughness. Over the land, r_c, the major component of v_d, is classified into stomatal-mesophyll resistance (r_s and r_m), cuticular resistance (r_{lu}), in-canopy resistance (r_{dc} and r_{cl}), and ground resistance (r_{ac} and r_{gs}):

$$r_c = \frac{1}{\left[\frac{1}{r_s+r_m}+\frac{1}{r_{lu}}+\frac{1}{r_{dc}+r_{cl}}+\frac{1}{r_{ac}+r_{gs}}\right]} \qquad \text{(S4)}$$

where r_{dc} is resistance for gas-phase transfer affected by buoyant convection in the canopy when sunlight heats the (near-)surface, r_{cl} is resistance for leaves, twigs, bark, and others in the lower canopy, r_{ac} is resistance for transfer that depends mostly on canopy structure, and r_{gs} is resistance for soil, leaf litter, snow, and others at the ground surface.

r_c is usually strongly affected by its stomatal-mesophyll resistance term which is expressed as seasonal- and land use/cover-dependent constants being adjusted by surface radiation and temperature (for 40 °C $\geq$ temperature $\geq$0 °C conditions). For calculating the other terms of r_c, prescribed seasonal- and land use/cover-dependent constants are used, with r_{lu} over dry surfaces (according to the modeled humidity and precipitation fields) adjusted by surface temperature and r_{dc} adjusted by surface radiation. A temperature-dependent term is also added to r_{lu}, r_{cl}, and r_{gs} to approximate an effect that coldness sometimes reduces the uptake. Figure S6 shows the base case results of $\frac{1}{r_s+r_m}$, $\frac{1}{r_{lu}}$, and $\frac{1}{r_{dc}+r_{cl}} + \frac{1}{r_{ac}+r_{gs}}$, as well as the SMAP DA impacts on these model fields. The captions of Figures S1 and S7 describe how the omission of soil moisture and vapor pressure deficit may have affected the evaluation of SMAP DA impacts on the modeled r_s and v_d.

References (cited in this document but not in the main text)

Convention on Long-Range Transboundary Air Pollution (CLRTAP): Mapping Critical Levels for Vegetation, Chapter 3 of Manual for modelling and mapping critical loads and levels, available at: https://www.umweltbundesamt.de/en/manual-for-modelling-mapping-critical-loads-levels (last access: December 2020), 2017.

Kennedy, A. D., Dong, X., Xi, B., Xie, S., Zhang, Y., and Chen, J.: A Comparison of MERRA and NARR Reanalyses with the DOE ARM SGP Data, J. Climate, 24, 4541–4557, doi:10.1175/2011JCLI3978.1, 2011.

LeMone, M. A., Tewari, M., Chen, F., Alfieri, J. G., and Niyogi, D.: Evaluation of the Noah land surface model using data from a fair-weather IHOP_2002 day with heterogeneous surface fluxes, Mon. Weather Rev., 136, 4915–4941, doi:10.1175/2008MWR2354.1, 2008.

Niu, G.-Y., Yang, Z.-L., Mitchell, K. E., Chen, F., Ek, M. B., Barlage, M., Kumar, A., Manning, K., Niyogi, D., Rosero, E., Tewari, M., and Xia, Y.: The community Noah land surface model with multiparameterization options (Noah-MP): 1. Model description and evaluation with local-scale measurements, J. Geophys. Res., 116, D12109, doi:10.1029/2010JD015139, 2011.

Rodell, M., Houset, P. R., Berg, A. A., and Famiglietti, J. S.: Evaluation of 10 Methods for Initializing a Land Surface Model, J. Hydrometeorol., 6, 146–155, doi:10.1175/JHM414.1, 2005.

Royer, A. and Poirier, S.: Surface temperature spatial and temporal variations in North America from homogenized satellite SMMR-SSM/I microwave measurements and reanalysis for 1979–2008, J. Geophys. Res., 115, D08110, doi:2009JD012760, 2010.

Wang, Z., Zeng, X., and Decker, M.: Improving snow processes in the Noah land model, J. Geophys. Res., 115, D20108, doi:10.1029/2009JD013761, 2010.
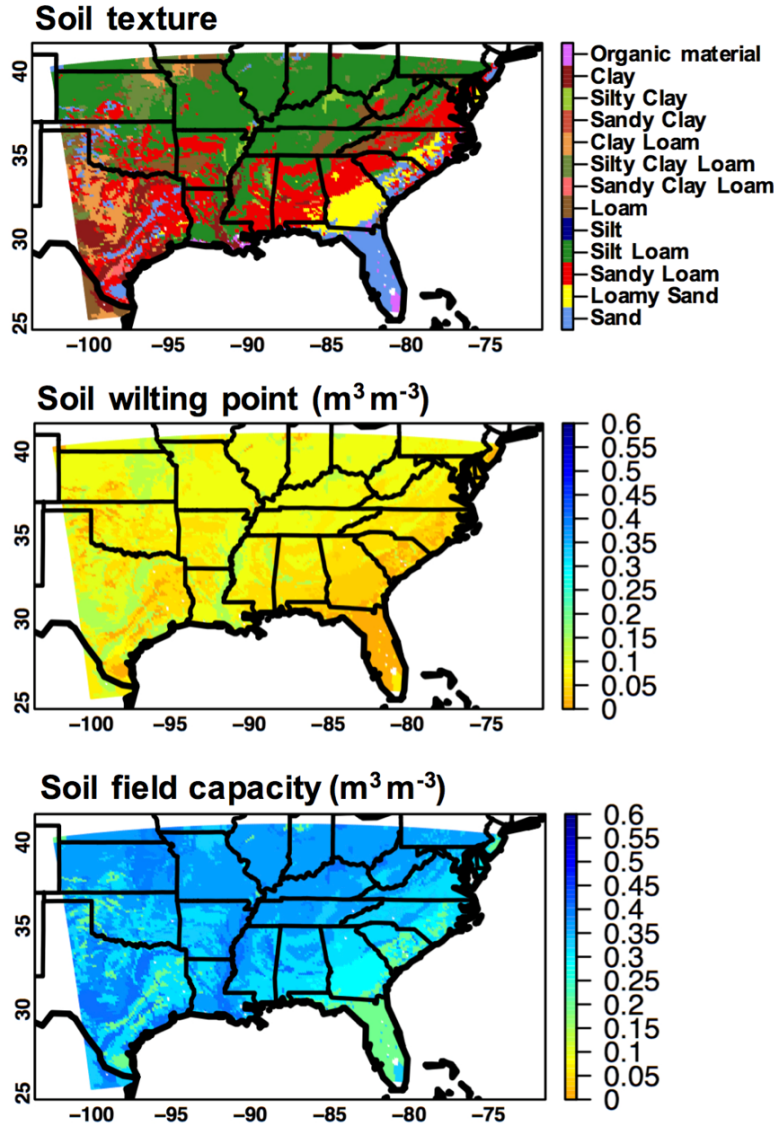
Figure S1. Grid-dominant (upper) soil texture types; (middle) soil wilting point; and (lower) soil field capacity used in the 12 km LIS/WRF-Chem simulations. The soil wilting points and field capacities are determined from the soil texture types and a soil parameter lookup table.

In the Jarvis-type of parameterizations, a soil moisture (SM) limitation factor f_{sm}^{-1} ($f_{sm} = \min\left[1, \max\left(f_{min}, \frac{SM - \text{Wilting point}}{\text{Field capacity} - \text{Wilting point}}\right)\right]$, where f_{min} is slightly above 0), which ranges from f_{min} (dry) to 1 (wet), is used to adjust the stomatal resistance r_s in the Noah land surface model. This type of adjustment to the modeled r_s has also been applied to deposition calculations in chemical transport models (e.g., Anav et al., 2018). f_{sm} is calculated based on SM from a given soil layer between the surface and the root zone which depends on land use/cover, and alternatively, it can be based on the maximum or column-averaged SM within these soil layers. Including such a SM limitation factor may not necessarily improve the modeled r_s or/and deposition velocity partially due to the uncertainty in the model's land use/cover input and the prescribed constant values in these algorithms.
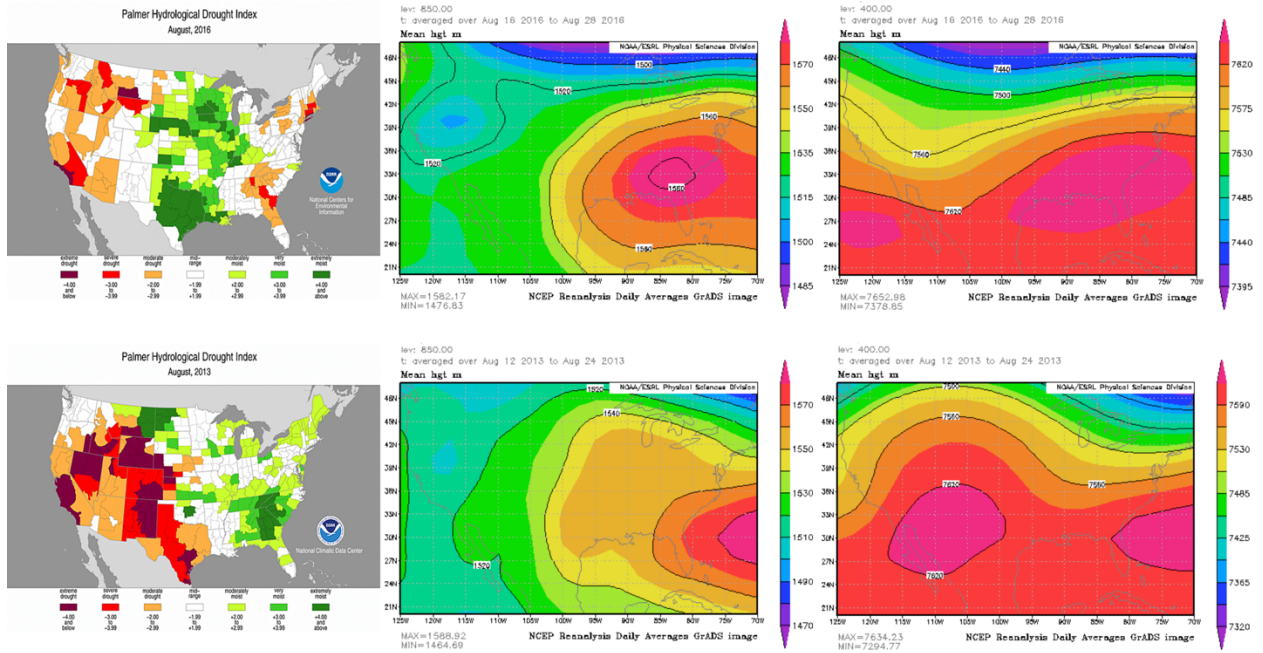
4

Figure S2. Drought and synoptic conditions in August 2016 and August 2013: (left) Palmer Hydrological Drought Index in August 2016 and August 2013; (middle) 850 hPa geopotential heights during 16-28 August 2016 and 12-24 August 2013; and (right) 400 hPa geopotential heights during 16-28 August 2016 and 12-24 August 2013. Data sources: National Climatic Data Center for the drought index and NCEP/NCAR reanalysis for geopotential heights.
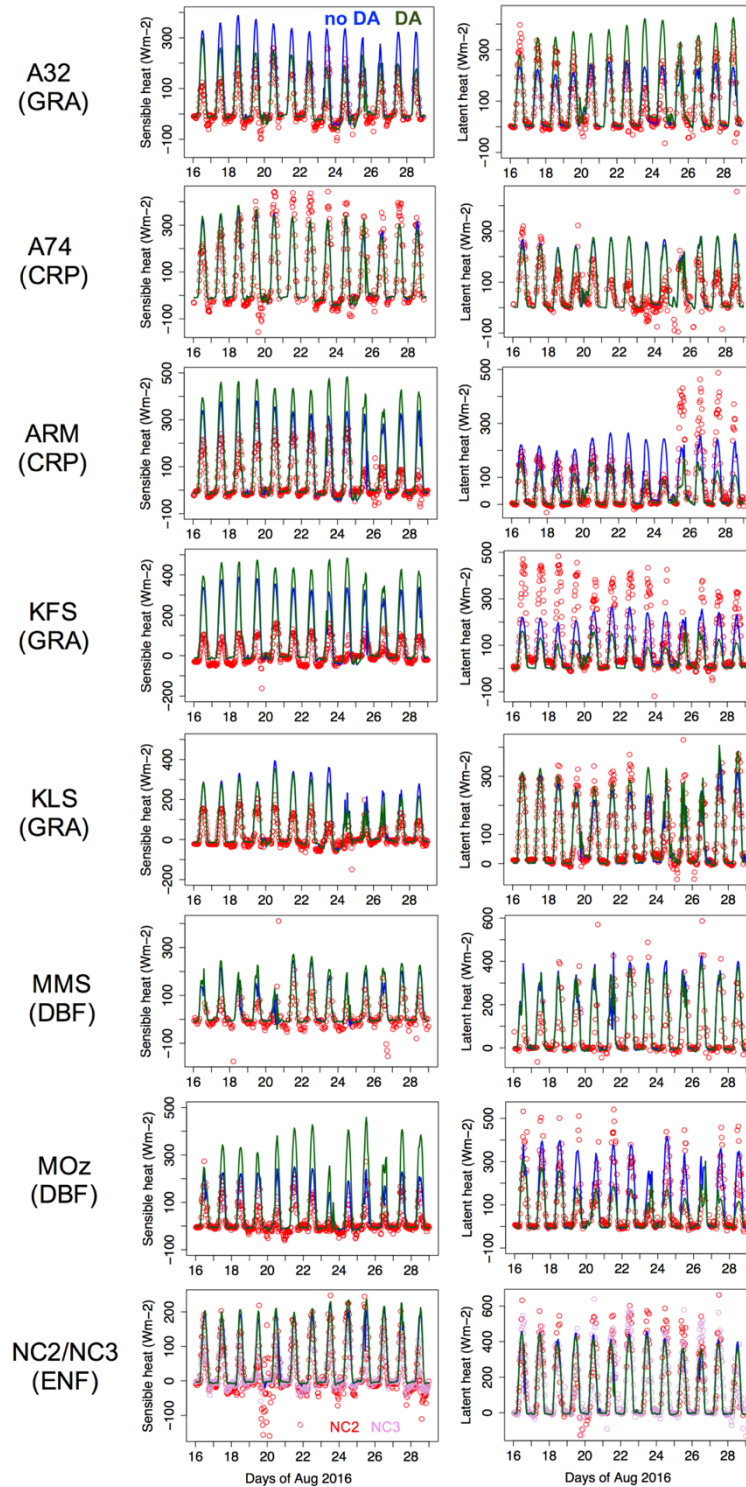
Figure S3. Evaluation of WRF-Chem modeled (left) sensible and (right) latent heat fluxes at selected FLUXNET sites shown in Figure 6b. Observations, base case and the "assim" case results are shown in red/pink open circles, blue and green solid lines, respectively. Acronyms of the land cover classifications of these sites are included in parentheses below the site names: GRA: grassland; CRP: cropland; DBF: deciduous broadleaf forests; ENF: evergreen needleleaf forests. Observation frequency is hourly at MMS and half-hourly at the other sites.

6
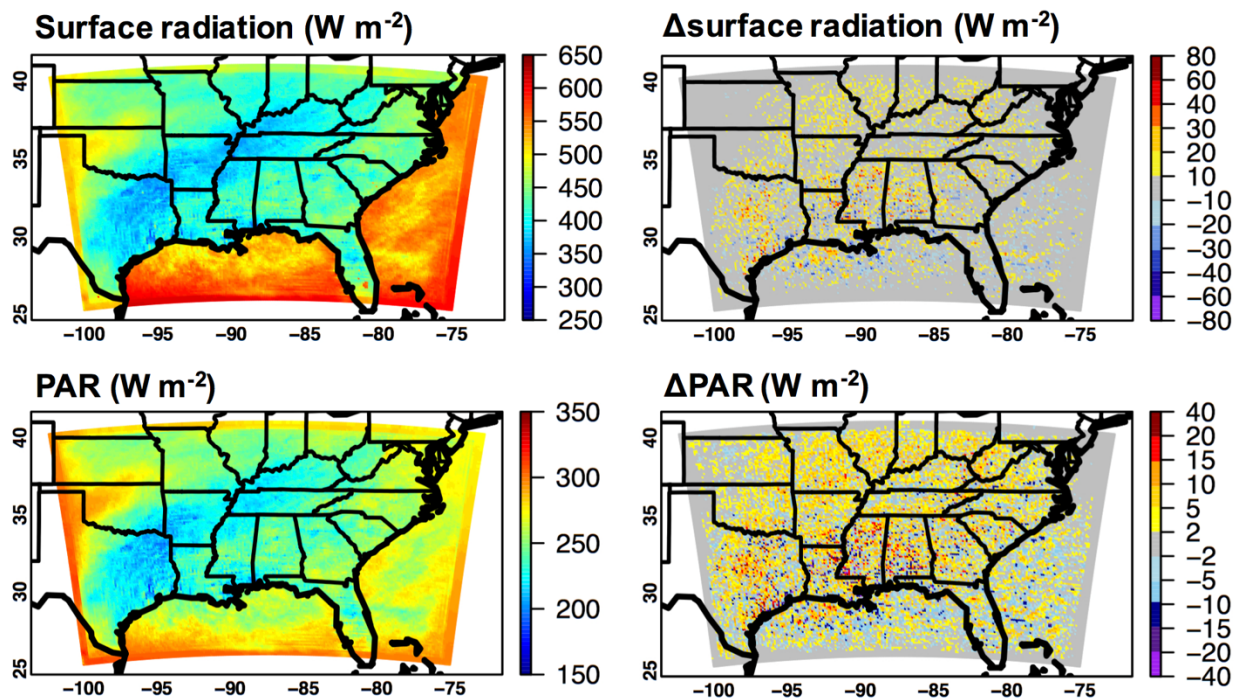
Figure S4. Period-mean (16-28 August 2016) WRF-Chem daytime (upper) surface radiation and (lower) photosynthetically active radiation (PAR). The left panels are base case results, and the SMAP DA impacts on these model fields are shown in the right panels. Surface radiation and PAR are required inputs for dry deposition and biogenic emission calculations, respectively.
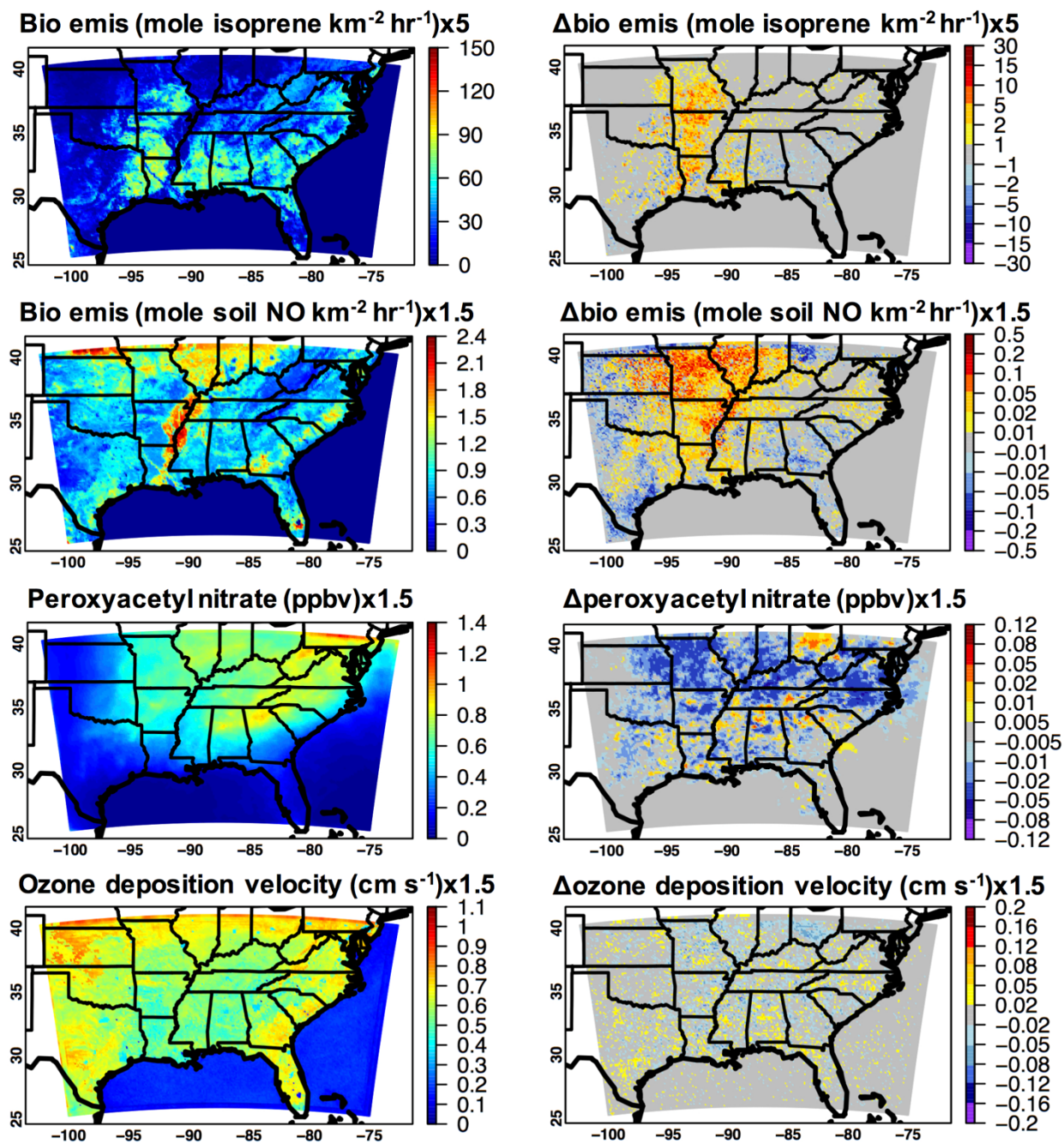
Figure S5. Period-mean (16-28 August 2016) WRF-Chem early morning (12 UTC)/evening (00 UTC) biogenic emissions of (upper) isoprene and (row 2) soil NO; (row 3) surface peroxyacetyl nitrate concentration; and (lower) O_3 deposition velocity. The left panels are the base case results, and the SMAP DA impacts on these model fields are shown in the right panels. Results shown here and in Figure 9 indicate strong diurnal cycles in these model fields as well as their responses to the SMAP DA.
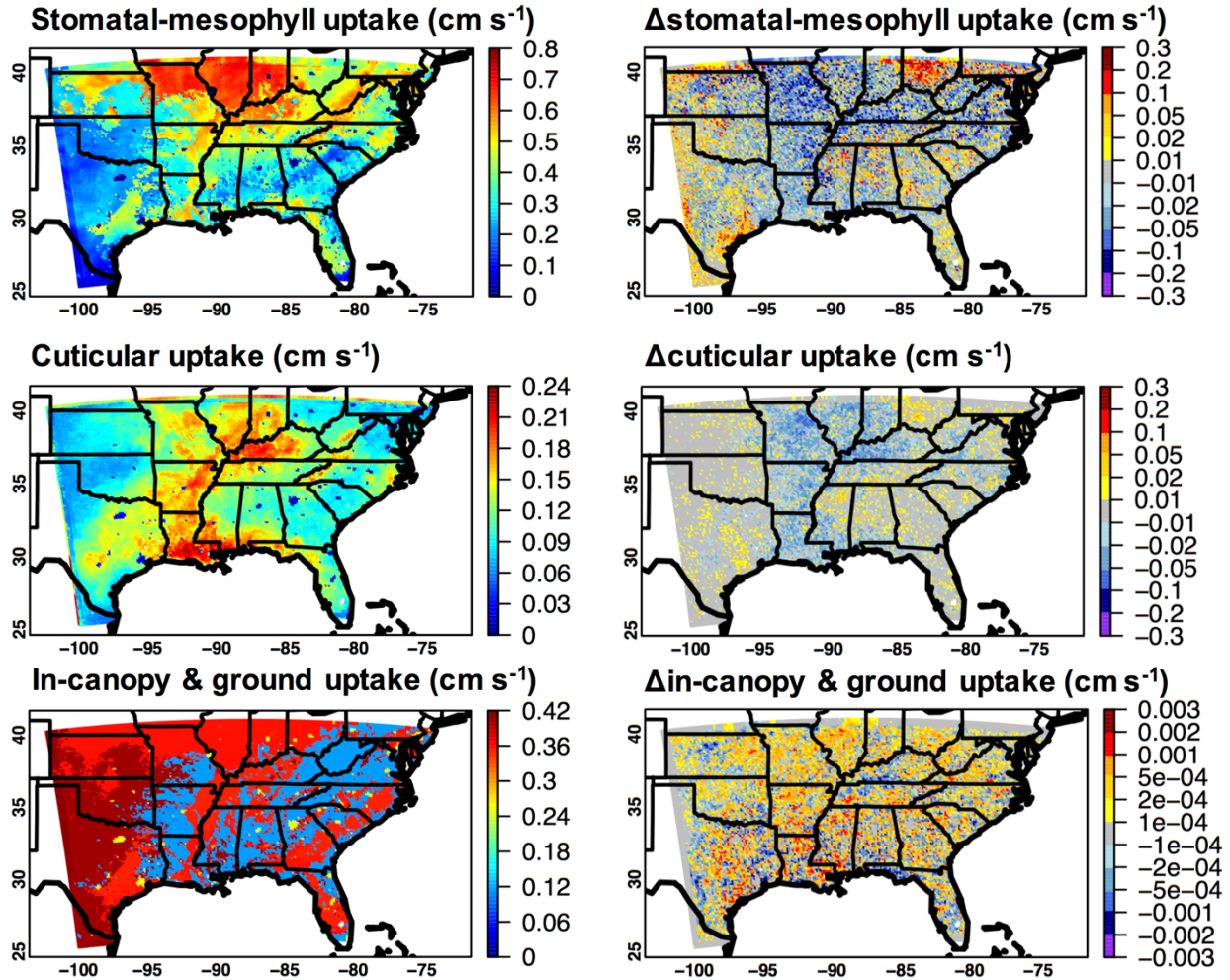
Figure S6. Period-mean (16-28 August 2016) WRF-Chem daytime (upper) stomatal-mesophyll uptake $\frac{1}{r_s+r_m}$; **(middle) cuticular uptake** $\frac{1}{r_{lu}}$; **and (lower) in-canopy and ground uptake** $\frac{1}{r_{dc}+r_{cl}} + \frac{1}{r_{ac}+r_{gs}}$, **in overland model grids. These terms, as well as their sensitivities to various environmental variables, are defined in Section S2. The left panels are base case results, and the SMAP DA impacts on these model fields are shown in the right panels.**
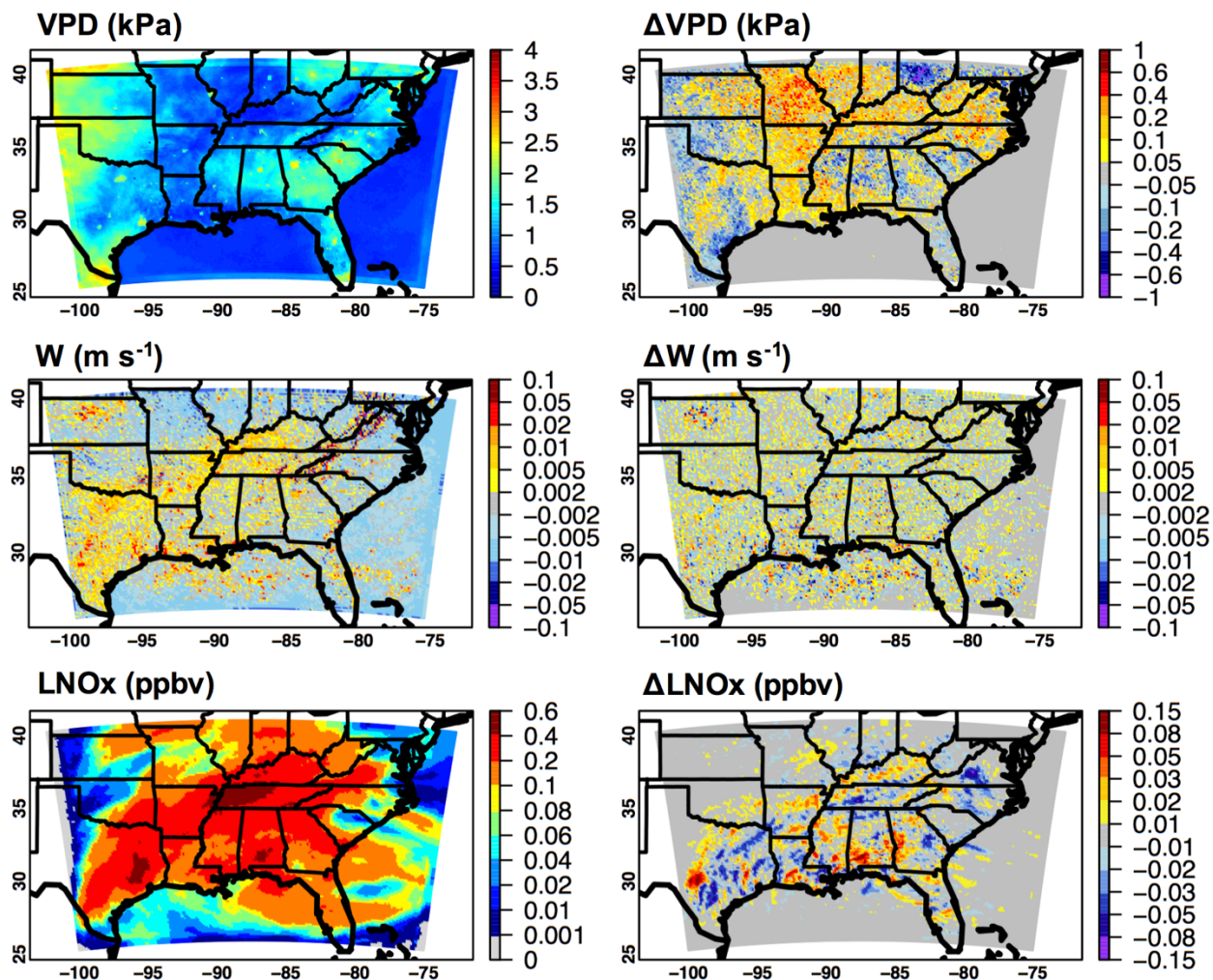
9

Figure S7. Period-mean (16-28 August 2016) WRF-Chem daytime (upper) surface vapor pressure deficit, VPD; (middle) vertical wind speed W averaged from surface level to ~200 hPa, with noises near the domain boundaries screened; and (lower) lightning NO_x (LNO_x) tracer results at ~400 hPa. The left panels present the base case results, and the SMAP DA impacts on these model fields are shown in the right panels.

The spatial patterns the modeled VPD responses to the SMAP DA are overall correlated with those of the modeled 2 m air temperature, which are anti-correlated with the model's RH responses. A VPD limitation factor f_{VPD}^{-1}

$$\left(f_{VPD} = \min\left[1, \max\left(f_{min}, \frac{(1-f_{min}) \times (VPD_{min} - VPD)}{VPD_{min} - VPD_{max}} + f_{min}\right)\right]\right)$$

is used in other studies to adjust the stomatal resistance term r_s in dry deposition calculations (Chapter 3 of the Convention on Long-Range Transboundary Air Pollution, CLRTAP, 2017). If this limitation factor was included in this work, the modeled dry deposition velocities in the base case would decrease in places. For high VPD regions (e.g., >1 kPa), depending on the land cover type, the stomata-related reductions may reach ~50% (referring to the f_{VPD} − stomatal conductance relationships in Figure III.7 of CLRTAP, 2017). Also, the modeled deposition velocities may respond more intensely to the SMAP DA.
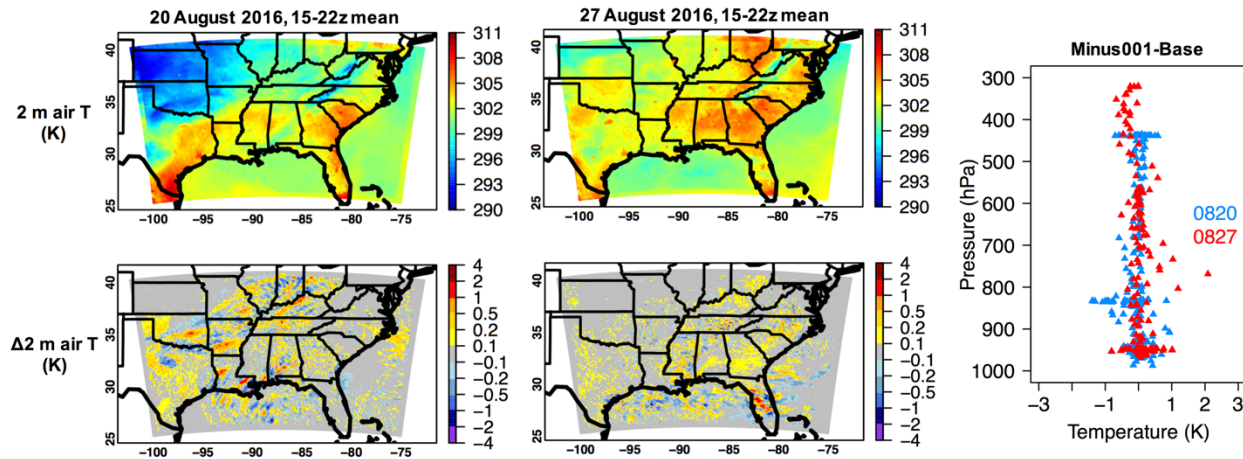
Figure S8a. (left and middle) WRF-Chem 2 m air temperature fields during 15-22 UTC of 20 and 27 of August 2016, as well as their responses to uniformly reducing the surface SM initial conditions by 0.01 m³m⁻³. (right) WRF-Chem air temperature changes along two ACT-America B-200 flights in response to this SM reduction. These two B-200 flights were conducted during approximately 15-22 UTC of 20 August 2016 and 18-22 UTC of 27 August 2016, respectively. The flight paths and altitudes are shown in Figure S8b.
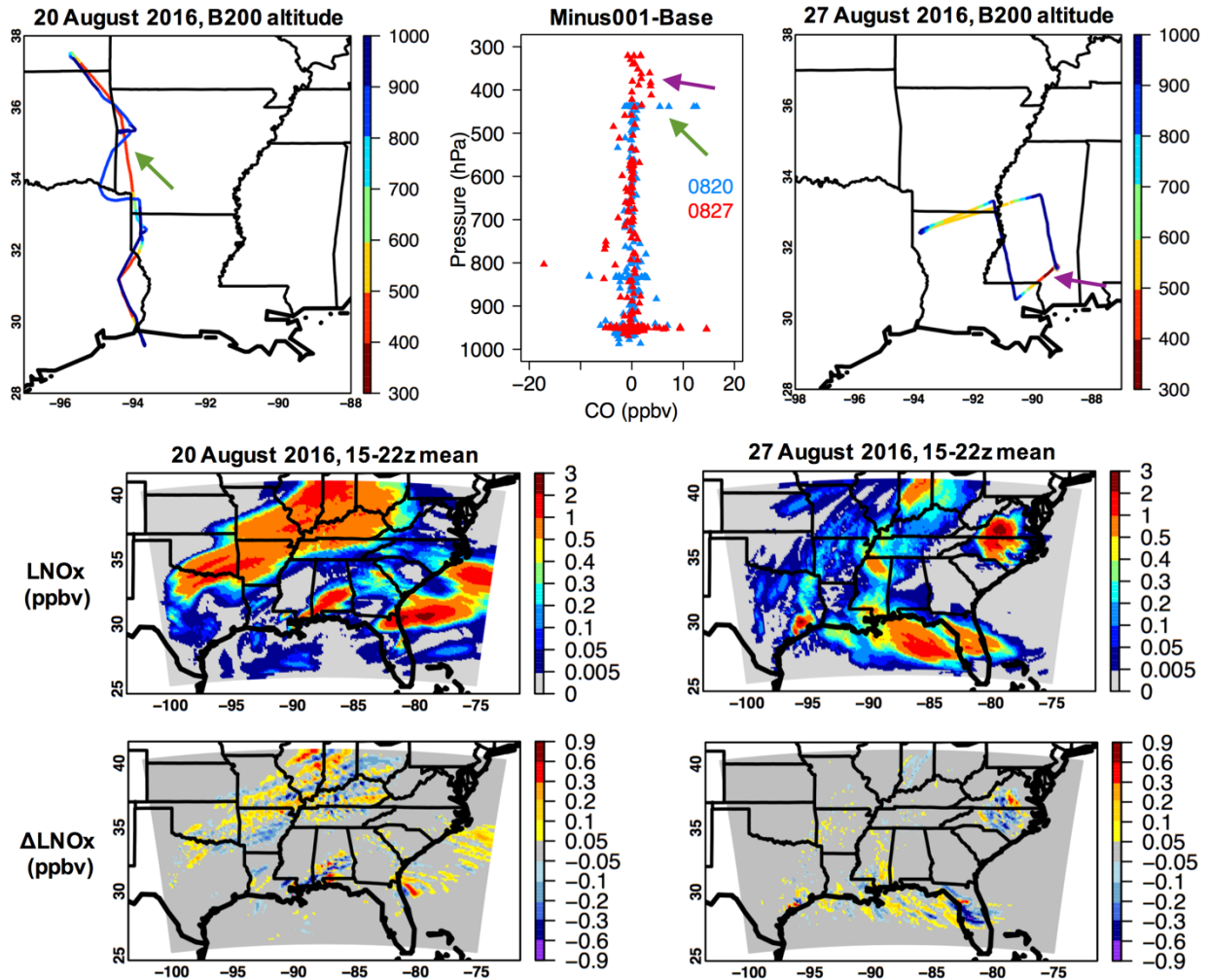
Figure S8b. (upper) ACT-America B-200 flight paths on 20 and 27 of August 2016, colored by flight altitudes in hPa, together with WRF-Chem CO changes along these flights in response to the SM reduction. (middle and lower) WRF-Chem lightning NO$_x$ (LNO$_x$) tracer results at ~400 hPa during 15-22 UTC of 20 and 27 of August 2016, as well as their responses to the SM reduction. The green and purple arrows in the upper panels denote the cold front- and/or convection-affected regions sampled by the B-200, on 20 and 27 of August 2016, respectively, as well as the WRF-Chem modeled CO sensitivities over these regions.
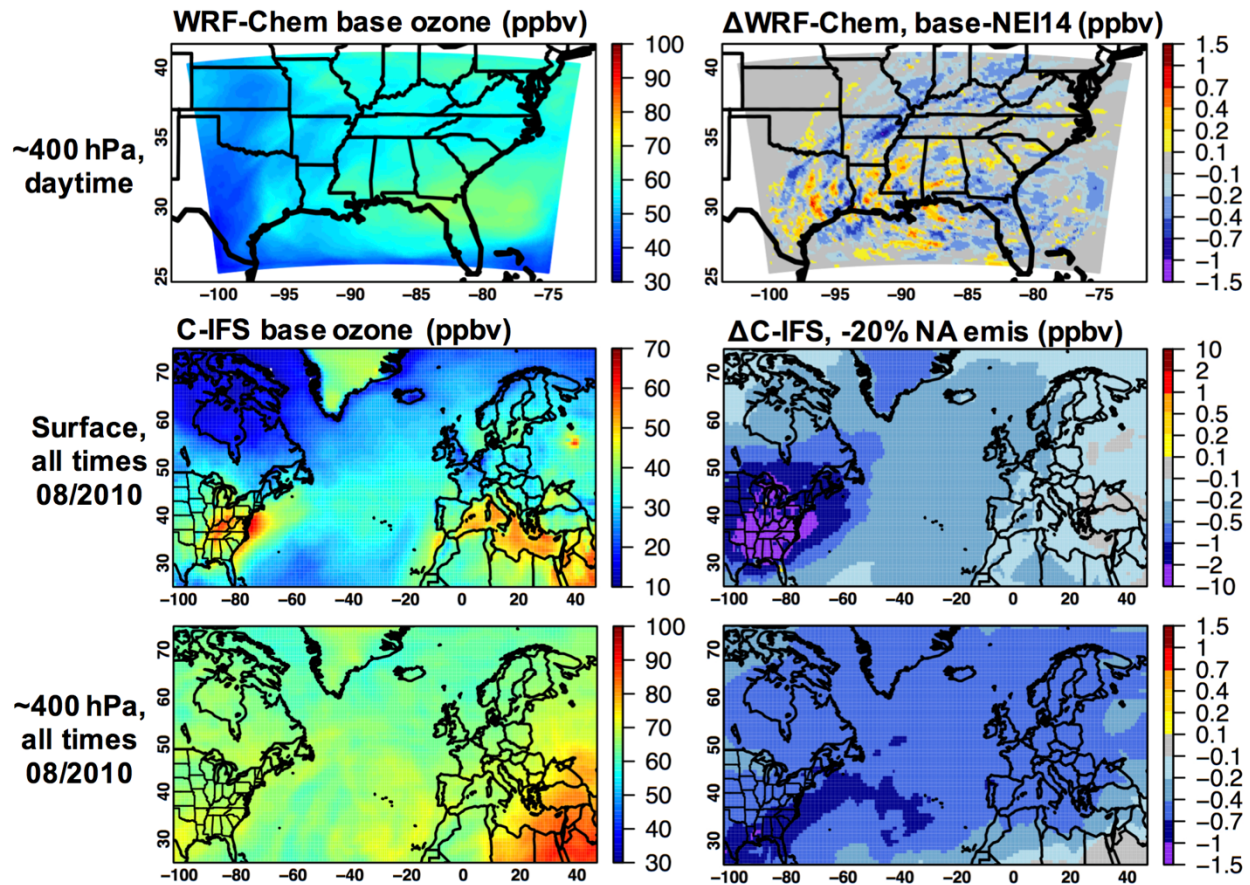
Figure S9. (left) O₃ and (right) impacts of emission changes on O₃ from: (upper) WRF-Chem at ~400 hPa, during the daytimes of 16-28 August 2016; (middle) the Composition-Integrated Forecasting System (C-IFS) at the surface, during all times of August 2010; and (lower) the C-IFS at ~400 hPa, during all times of August 2010. These C-IFS simulations were performed at 0.7°×0.7° in support of the HTAP Phase 2 (Huang et al., 2017a) multi-model experiments. "NA" in the center-right panel stands for "North American".
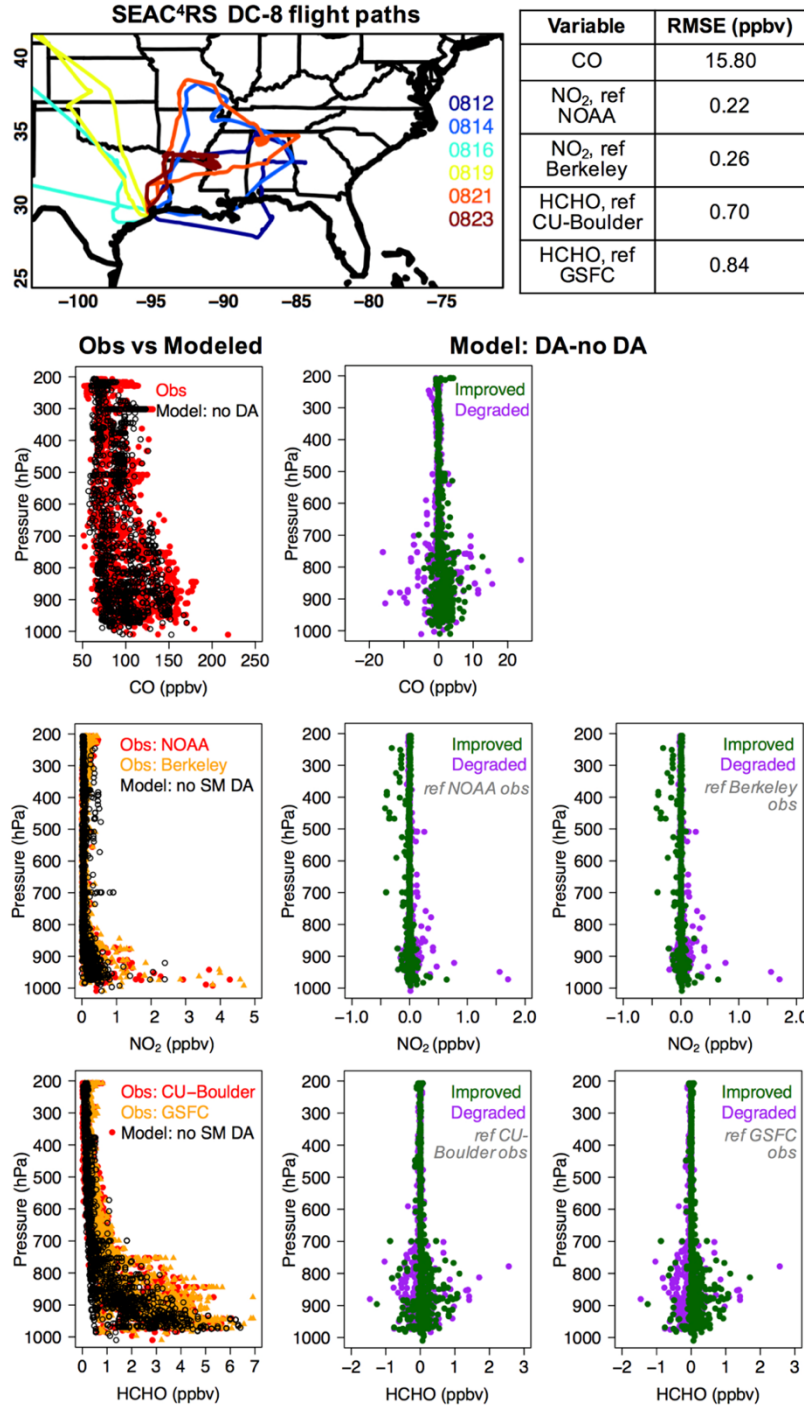
Figure S10. Evaluation of WRF-Chem modeled CO, NO₂, and HCHO with the DC-8 aircraft observations during six SEAC⁴RS flights in August 2013. The upper panel shows the related fight paths, together with model performance in the "SEACf" case. Correlation coefficients *r* between the modeled and observed CO, NO₂ and HCHO are: 0.8, 0.6, 0.9, respectively. The other panels present 1-minute averaged observations along with their WRF-Chem counterparts from the "SEACf" case and the differences between the "SEACa" and "SEACf" cases. Whether the SM DA improved or degraded the model performance is indicated in the "DA-no DA" (i.e., SEACa-SEACf) difference plots.

14